Magn Reson Mater Phy (2016) 29:347–358
DOI 10.1007/s10334-016-0545-4

RESEARCH ARTICLE

3D T_2-weighted imaging at 7T using dynamic k_T-points on single-transmit MRI systems

Florent Eggenschwiler[1] · Kieran Robert O'Brien[2,3] · Daniel Gallichan[1] · Rolf Gruetter[1,4] · José Pedro Marques[5]

Received: 2 November 2015 / Revised: 1 March 2016 / Accepted: 3 March 2016 / Published online: 8 April 2016

Abstract
Objectives For turbo spin echo (TSE) sequences to be useful at ultra-high field, they should ideally employ an RF pulse train compensated for the B_1^+ inhomogeneity. Previously, it was shown that a single k_T-point pulse designed in the small tip-angle regime can replace all the pulses of the sequence (static k_T-points). This work demonstrates that the B_1^+ dependence of T_2-weighted imaging can be further mitigated by designing a specific k_T-point pulse for each pulse of a 3D TSE sequence (dynamic k_T-points) even on single-channel transmit systems
Materials and methods By combining the spatially resolved extended phase graph formalism (which calculates the echo signals throughout the sequence) with a gradient descent algorithm, dynamic k_T-points were optimized such that the difference between the simulated signal and a target was minimized at each echo. Dynamic k_T-points were inserted into the TSE sequence to acquire in vivo images at 7T.
Results The improvement provided by the dynamic k_T-points over the static k_T-point design and conventional hard pulses was demonstrated via simulations. Images acquired with dynamic k_T-points showed systematic improvement of signal and contrast at 7T over regular TSE—especially in cerebellar and temporal lobe regions without the need of parallel transmission.
Conclusion Designing dynamic k_T-points for a 3D TSE sequence allows the acquisition of T_2-weighted brain images on a single-transmit system at ultra-high field with reduced dropout and only mild residual effects due to the B_1^+ inhomogeneity.

Keywords T_2-weighted imaging · B_1^+ inhomogeneity correction · Dynamic k_T-points · TSE sequence · Spatially resolved extended phase graph

Introduction

T_2-weighted imaging is a very common clinical imaging contrast; amongst other applications, it plays a crucial role in the detection of gray and white matter lesions such as in multiple sclerosis [1, 2], Alzheimer's disease [3], and cancer [4]. This imaging technique should benefit from the increased signal-to-noise ratio (SNR) available at high field strengths ($B_0 \geq 3$T), allowing acquisitions with higher spatial resolution and hence better visualization of small brain structures. While most clinical applications using TSE contrast are based on 2D TSE and anisotropic voxels (to ensure whole brain coverage within SAR constraints and in clinical acceptable times), remarkable image quality at quasi-isotropic spatial resolution has been demonstrated at 7T using various 2D TSE implementations [5], but these have been limited to small z-coverage (~21 mm). One approach to overcome these limitations is the use of simultaneous multi-slice imaging combined with PINS pulses to reduce

✉ Florent Eggenschwiler
florent.eggenschwiler@epfl.ch

1 Laboratory for Functional and Metabolic Imaging, Ecole Polytechnique Fédérale de Lausanne, Station 6, 1015 Lausanne, Switzerland

2 Centre for Advanced Imaging, University of Queensland, Brisbane, Australia

3 Siemens Healthcare Pty Ltd, Brisbane, QLD, Australia

4 Department of Radiology, Universities of Lausanne and Geneva, Vaud, Switzerland

5 Donders Center for Cognitive Neuroimaging, Radboud University, Nijmegen, The Netherlands

SAR [6] or 3D-TSE implementations with long RF pulse trains. The presence of spatial B_1^+ inhomogeneities at high field results in signal voids and different degrees of contrast between tissues throughout the volume as has been reported and is visible in several studies [5, 7–9]. Sequences involving a 3D TSE readout such as the fluid-attenuated inversion recovery (FLAIR) and the double inversion recovery (DIR) are now frequently used in clinical routines; however, usefulness of such sequences is limited by the non-uniform B_1^+ profile that propagates throughout the train of RF pulses.

In a previous study [10], improved-quality whole-brain T_2-weighted imaging was achieved by replacing the original hard pulses of a 3D TSE sequence with k_T-point [11] pulses. For both single and parallel transmit systems, a single k_T-point pulse was designed in the small tip-angle regime with a uniform excitation profile as a target. Each pulse of the 3D TSE sequence with variable flip-angle was replaced by the designed k_T-point pulse, which had fixed amplitude and phase relationships between the sub-pulses. This configuration will be referred to as a static k_T-point design in the current paper.

Instead of searching for the most uniform excitation profile, another approach was recently proposed [12] that directly optimized the signal throughout the TSE sequence on a parallel transmission (PTx) system. The spatially varying B_1^+ profile of the different channels was incorporated into the methodology by considering a spatially resolved extended phase graph (SR-EPG) to provide a simulation of all the states of the magnetization across the sequence for each voxel in the brain. The inverse problem of computing specific amplitudes and phases of the different array elements for each pulse lead to the expected signal response for all the echoes throughout the sequence by taking advantage of the extra degrees of freedom provided by PTx. Since amplitude and phase relationships between channels vary from pulse to pulse, this methodology was presented as a "dynamic" RF shimming. This concept has been extended to the incorporation of different k_T-points throughout the echo train [13] where the optimization was based on gradient ascent combined with optimal control, and the rotation matrix describing the effect of each k_T-point pulse for each channel was optimized. Such an approach will be named in the current manuscript as dynamic k_T-points. While the study demonstrated improved image quality, the use of PTx is not a widely available technology in 7T clinical environments, as it requires the mastering of complex hardware as well as the subject/RF pulse specific absorption rate (SAR) modeling.

The aim of this article is to demonstrate that T_2-weighted imaging at 7T can be improved by designing a specific k_T-point pulse for each pulse of a 3D TSE sequence with variable flip angles, even when operating with a single-channel transmit RF system. In the methodology presented here, the magnetization across the TSE sequence is simulated and optimized by making use of the SR-EPG framework. Additionally, a higher flexibility was obtained by separately optimizing the k-space points visited by the excitation pulse where the number of designed k_T-points was higher than for the refocusing pulses. The impact of the chosen cost function used in the optimization algorithm was also investigated.

Materials and methods

Design of dynamic k_T-points

As proposed in [14], a 3D TSE sequence with a train of modulated flip-angles was used in order to bring the magnetization into a static pseudo-steady state (sPSS) and then maintain it throughout a large number of echoes such that image artifacts are minimized. Accordingly, the flip-angles $[\alpha_1^{\text{nom}},\ldots, \alpha_{\text{ETL}}^{\text{nom}}]$ were optimized depending on the parameters of the sequence and specified T_1/T_2 relaxation times (Fig. 1a, red and black dots). ETL represents the echo train length of the TSE sequence. Knowing the flip-angle train, the expected echo signal across the sequence $S^{\text{theo}} = [S_1^{\text{theo}},\ldots, S_{\text{ETL}}^{\text{theo}}]$ was simulated (Fig. 1a, blue dots) using a forward EPG formalism [15].

Given that the transmit magnetic field profile $B_1^+(\mathbf{r})$ varies throughout space at 7T, each flip-angle α_j in the train also becomes position dependent:

$$\alpha_j(\vec{r}) = B_1^+(\vec{r}) \cdot \alpha_j^{\text{nom}} \tag{1}$$

As mentioned previously, this inhomogeneity leads to signal and contrast variation since the signal at each echo becomes spatially varying. To correct for that, the original hard pulses of the sequence were replaced by k_T-point pulses, with their sub-pulse amplitudes and phases optimized such that the signal distribution for echoes throughout the sequence stays close to the theoretical value S^{theo} for all voxels belonging to the region of interest, Ω.

The dynamic k_T-point design thus consists of optimizing the amplitudes $A_{i,j}$ and phases $\varphi_{i,j}$ of sub-pulse i belonging to the jth k_T-point pulse ($j = 0$–ETL). The number of sub-pulses in the excitation and refocusing k_T-point pulses are given by n_{exc} and n_{ref}, respectively (Fig. 1b). The index $j = 0$ refers to the excitation pulse, i.e. $\alpha_0^{\text{nom}} = 90°$ (Fig. 1b).

Using the SR-EPG, the echo signal throughout all the voxels $S_p(\mathbf{r})$ can be simulated after each pulse p. The set of echoes for a sequence of ETL pulses was defined as $S(\mathbf{r}) = [S_1(\mathbf{r}),\ldots, S_{\text{ETL}}(\mathbf{r})]$ and is a function of the flip-angles (defined by the $A_{i,j}$ and $\varphi_{i,j}$ of the k_T-point pulses), which are position dependent due to the non-uniform B_1^+ profile.

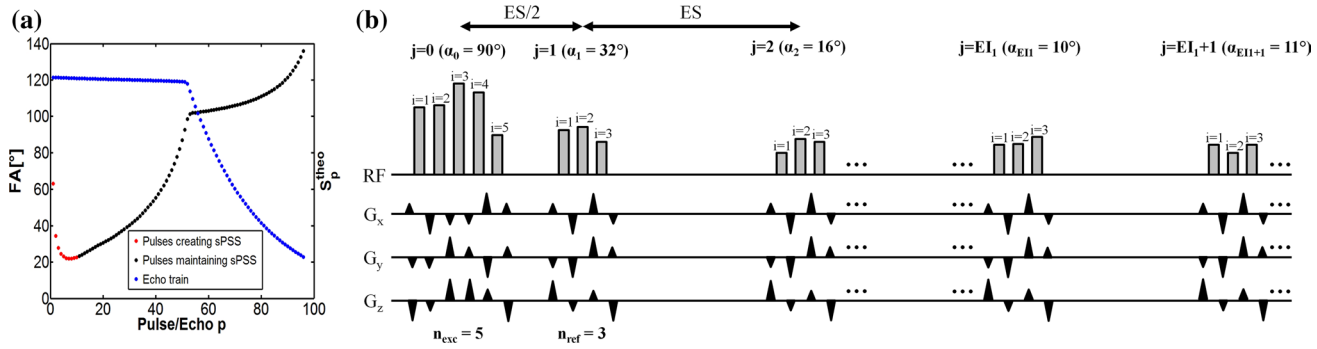

Fig. 1 **a** Signal at each echo of the 3D TSE sequence simulated for protocol A (ETL = 96) and assuming no B_1^+ inhomogeneity. *Red dots* correspond to the pulses bringing the magnetization into the sPSS which is maintained by the subsequent pulses (represented by *black dots*). The train of flip angles was optimized for specific T_1/T_2 relaxation times such that the sPSS is maintained over a large number of echoes. The echo train (*blue dots*) is presented in arbitrary units. **b** 3D TSE sequence with dynamic k_T-points. Example with $n_{exc} = 5$ and $n_{ref} = 3$ sub-pulses. In each k_T-point pulse, identified by the index j, the sub-pulses are identified by the index i which runs from 1 to n_{exc} for the excitation pulse and from 1 to n_{ref} for the refocusing pulses. The gradient blips of the excitation and refocusing k_T-point pulses are different since they were optimized using the linearization of the Bloch equations and the SOLO algorithm, respectively

The sub-pulse amplitudes and phases were thus optimized in order to minimize the difference between the simulated and theoretical signals $\sum_{i=1}^{EI} \left\| S_i(\vec{r}) - S_i^{theo} \right\|$ where EI refers to the echoes of interest, i.e. echoes involved in the optimization process. A gradient descent algorithm with a least-squares (LS) cost function was used to determine the $A_{i,j}$ and $\varphi_{i,j}$ providing the best match between the pairs $S_i(\mathbf{r})$ and S_i^{theo}.

The design of the dynamic k_T-point pulses for the whole sequence was performed in five steps:

- Step 1—As its efficiency in refocusing pathways was demonstrated [10], a symmetric k_T-point pulse with n_{ref} k_T-points was designed in the small tip-angle regime by using the sequential optimal selection of spokes (SOLO) algorithm [16] fed with the subject-specific B_1^+ profile. This pulse defined the k-space trajectory for all the refocusing pulses of the sequence.
- Step 2—An excitation pulse with n_{exc} k_T-points was designed in the high tip-angle regime by using a linearization of the Bloch equations [17]. The sub-pulse amplitudes and phases as well as the k-space trajectory were optimized in a LS sense in order to obtain a homogeneous excitation but also to match the phase profile corresponding to the one of the refocusing pulse created in step 1 such that the CPMG conditions were naturally fulfilled.
- Step 3—The amplitudes and phases of all the k_T-point sub-pulses of the first EI_1 refocusing pulses bringing the magnetization into the sPSS were optimized together such that the echo profiles $S(\mathbf{r}) = [S_1(\mathbf{r}),\ldots, S_{EI1}(\mathbf{r})]$ simulated using the SR-EPG match the theoretical signals $[S_1^{theo},\ldots,S_{EI1}^{theo}]$. With the sequence parameters used, EI_1 was set to 10 as shown in Fig. 1a (red dots). Steps 1 and 2 defined the starting conditions of this optimization.
- Step 4—The amplitudes and phases of the next pulses belonging to the sPSS (flat part on Fig. 1a) were optimized on a k_T-point pulse by k_T-point pulse basis ($EI_2 = 1$) by using the gradient descent algorithm. Here the goal was to maintain the signal homogeneity achieved at the end of step 3 for the remaining echoes of the sPSS. Each k_T-point had as initial guess the amplitudes and phases of the previously optimized k_T-point.
- Step 5—To limit the computational load, a static k_T-point design with the phase profile obtained at the end of step 4 was used for the refocusing pulses beyond the flat part of the sPSS (see Fig. 1).

The cost function, CF, of the gradient descent algorithm used in steps 3 and 4 was:

$$CF = \sum_{n=n_b}^{n_e} \left\| \left| S_n^{theo} e^{i\bar{\phi}} - S_n^c(\vec{r}) \right| \cdot B_1^+(\vec{r}) \right\|^{pow} \quad (2)$$

with n_b and n_e the indexes denoting the echoes involved in the optimization ($n_b = 1$; $n_e = EI_1$ in step 3 and $n_b = n_e =$ jth echo in step 4), c the current iteration and *pow* a power. A "traditional" least-squares approach corresponds to pow = 2, but it was found in the current implementation that higher values are useful to penalize solutions obtained when a small region of $S^c(\mathbf{r})$ was significantly different from the expected signal S^{theo}. The average phase $\bar{\phi}$ over the $n_e - n_b + 1$ echoes calculated at iteration $c - 1$ was introduced to ensure a smooth phase transition from one echo to the next, which improved the quality of the data acquired (not shown). The subject-specific B_1^+ profile was used as a weighting factor such that the importance

of very low B_1^+ regions for which the algorithm cannot provide a correction are downplayed (in the regions of very low B_1^+ field it is impossible to obtain the desired magnetization without compromising both the SAR and the homogeneity elsewhere).

Experimental setup

In vivo scans were performed on a Siemens 7T whole-body research scanner (Siemens Healthcare, Germany) equipped with a head gradient insert (maximum gradient amplitude and slew rate of 80 mT/m and 333 T/m/s, respectively). A 32-channel coil (Nova Medical, USA) was used for image acquisition.

The experimental protocol was approved by the local ethics committee and five healthy subjects providing informed consent were scanned.

Dielectric pads were placed below the top part of the neck for all subjects to increase the B_1^+ field in the cerebellar regions [18, 19].

B_1^+-mapping protocol

The transmit sensitivity profile $B_1^+(\mathbf{r})$ was obtained by acquiring an absolute B_1^+ map of the subject's brain using the SA2RAGE sequence [20] with the following parameters: TR = 2.4 s, TE = 1.35 ms, TD_1 = 50 ms, TD_2 = 1800 ms, $\alpha_1 = 4°$, $\alpha_2 = 11°$, $3.2 \times 3.2 \times 4.0$ mm^3 resolution and a $64 \times 64 \times 48$ matrix size acquired with sagittal orientation (acquisition time of 1 min 28 s).

Reduction of simulation space

The region of interest, Ω, where a matching between S^{theo} and the actual signal is desired was determined from a subject-specific brain mask. Because the computation time required for the calculation of dynamic k_T-point pulses is proportional to the number of voxels involved, the option of randomly using a subset of N_{vox} voxels inside the mask was investigated. This approach was chosen over simply creating lower resolution B_1^+ maps to avoid ringing artefacts and partial volume artifacts that would be otherwise introduced close to the edges. The aim of this analysis was to find a tradeoff between the computation time and the deviation made with respect to the solution obtained when considering all voxels in the mask. Values ranging from 75 to 2000 were tested for N_{vox} for a region Ω made of 4070 voxels.

Dynamic k_T-point evaluation

The SR-EPG framework was used to simulate the signal throughout the 3D TSE sequence when using: (1) standard hard pulses, (2) static k_T-point pulses, and (3) dynamic k_T-point pulses. When using the SR-EPG to calculate the evolution of the magnetization states, the sequence was simulated over $5 \cdot \text{TR}$ periods to ensure that the magnetization reached the steady-state.

The design of static k_T-points corresponds to step 1 in the dynamic k_T-point optimization process.

The quality of each approach was evaluated in terms of signal fidelity by calculating the following quantity throughout the entire sequence:

$$\text{DEV}_p = \frac{\left\| \left| S_p(\vec{r}) \right| - \left| S_p^{\text{theo}} \right| \right\|}{\left\| S_p^{\text{theo}} \right\|} \tag{3}$$

where p refers to the echo number. Another signal homogeneity assessment was performed by computing the spatial standard deviation STDev_p across each $S_p(\mathbf{r})$ map. In this way, only the homogeneity and not the deviation from the desired echo train was evaluated.

For static k_T-points, simulations were performed with $N = 3$ and $N = 5$ k_T-points, where N corresponds to the number of k_T-points of each sequence pulse. These simulations were compared with the SR-EPG profiles calculated for the dynamic k_T-points where $n_{\text{exc}} = 5$ and $n_{\text{ref}} = 3$ were used.

Turbo spin echo protocol

The T_2-weighted images were acquired with a commercially available variable flip-angle 3D TSE sequence known as the sampling perfection with application optimized contrasts using different flip angle evolutions (SPACE) sequence [5]. This sequence optimizes the signal evolution of the flip angle train for specified T_1/T_2 relaxation times and allows longer RF-pulse trains to be used making it possible to efficiently acquire 3D TSE images. In this work, T_1 and T_2 were set to their average value at 7T for brain tissues, i.e. 1400 and 60 ms, respectively.

Replacing the original hard pulses of the 3D TSE sequence with variable flip angles by sets of sub-pulses and gradient blips increases the SAR of the sequence. A tradeoff between the SAR constraints and the GM-WM contrast was thus considered to establish the basic sequence parameters. Three different protocols were used for the acquisitions of T_2-weighted images, generating different degrees of signal and contrast variations:

Protocol A—TR = 2.4 s, TE = 280 ms, ETL = 96, ES = 7.6 ms, RF_{Dur} = 3.0 ms, resolution = $0.7 \times 0.7 \times 0.7$ mm^3, matrix size = $320 \times 320 \times 224$, $n_{\text{exc}} = 5$ and $n_{\text{ref}} = 3$ k_T-points, RF sub-pulse duration = 540 µs (total acquisition time 7 min 50 s).

Protocol B—TR = 3.4 s, TE = 383 ms, ETL = 166, ES = 6.6 ms, RF_{Dur} = 2.5 ms,

resolution = 0.7 × 0.7 × 0.8 mm^3, matrix size = 320 × 320 × 224, $n_{exc} = 5$ and $n_{ref} = 3$ k_T-points, RF sub-pulse duration = 440 µs (total acquisition time 7 min 45 s).

Protocol C—TR = 2.7 s, TE = 364 ms, ETL = 166, ES = 6.6 ms, RF_{Dur} = 2.5 ms, resolution = 0.7 × 0.7 × 0.8 mm^3, matrix size = 320 × 320 × 192, $n_{exc} = 5$ and $n_{ref} = 3$ k_T-points, RF sub-pulse duration = 360 µs (total acquisition time 5 min 17 s).

The different protocols were used to demonstrate that the design of dynamic k_T-points to correct the typical signal and contrast variations in the brain caused by the B_1^+ inhomogeneity at 7T was robust against changes in sequence parameters.

For protocols A, B, and C, the duration of all the gradient blips was set to 60 µs. When optimizing the first part of the TSE train (step 3), $EI_1 = 10$ was used to evaluate the cost function. For protocols A, B, and C, 52, 75, and 80 dynamic k_T-points were optimized before inserting static k_T-points after the sPSS, respectively.

If a sub-pulse i in the dynamic k_T-point design exceeded the maximum RF voltage allowed by the scanner, it was split into n_s entities with the same RF duration as the other sub-pulses and separated by blank intervals without gradient blips. Because of constraints on the RF pulse objects used, this was mimicked by all the pulses of the sequence. The actual number of sub-pulses per k_T-point pulse was, therefore, $n_{ref} - 1 + n_s$. The values for n_s used in protocols A, B, and C were 3, 3, and 5, respectively.

The use of non-spatially selective RF pulses implied that all protocols were acquired in the sagittal direction, with the readout along the head to foot axis and both phase encoding directions had to cover the full head volume (as is commonly done for most 3D T_1-weighted imaging) to avoid wrap around artifacts.

Standard 3D TSE images with non-selective hard pulses (no k_T-points) and all parameters identical to those of protocols A, B, and C were acquired for comparison.

For the sake of simplicity, the B_0 inhomogeneity over the brain was not considered when optimizing static and dynamic k_T-points. To make a fair comparison between the T_2-weighted images acquired with different types of RF pulses, in the conventional case without k_T-points a hard pulse with the same duration as the k_T-point sub-pulses (540, 440, 360 µs for protocols A, B, and C, respectively) was used while maintaining the same echo spacing (to ensure the same T_2-weighted contrast). In this way, the impact of the B_0 inhomogeneity was similar on images acquired with and without k_T-points, and any improvements observed should be attributed to the B_1^+ compensation mechanism of the k_T-points.

To provide an indication of the image quality that can be obtained with dynamic k_T-points on other types of contrast, a FLAIR acquisition was performed with the 3D TSE sequence. This was done by adding an inversion pulse (a standard non-selective adiabatic inversion pulse provided by the manufacturer) at the beginning of the sequence. For this measurement, dynamic k_T-points combined with protocol C were used. The times TR and TI were set to 4 and 1.35 s to ensure the suppression of the CSF signal.

Data processing

To focus on the improvement provided by k_T-points in terms of contrast and signal homogeneity, bias field correction was applied to the anatomical images, in order to remove the signal variations related to the highly non-uniform reception profile $B_1^-(\mathbf{r})$ of the 32-channel coil. The bias field correction was performed using FAST (http://www.fsl.fmrib.ox.ac.uk), which calculates a smooth profile, mainly corresponding to $B_1^-(\mathbf{r})$ [21].

Results

Cost function considerations

Figure 2b shows that when the $B_1^+(\mathbf{r})$ profile (Fig. 2a) was not considered as a weighting term in Eq. 2 and with pow = 2, the optimization efforts regarding the correction of low B_1^+ regions created an intensity hole in the center of the magnetization profile. The last three columns of Fig. 2 illustrate how the hole formation can be avoided in the solution by increasing the value of pow (Fig. 2c, e) and by considering $B_1^+(\mathbf{r})$ as a weighting term (Fig. 2d, e) in Eq. 2. Note that using this weighting term and increasing pow slightly worsened the deviation with respect to the theoretical echo signal and the standard deviation (in a least-squares sense) across the magnetization profile (see the numbers on the bottom of Fig. 2), but this was negligible when compared to the benefit of not having the severe signal variation at the brain center. Moreover, the SAR of the optimized dynamic k_T-points remained similar or even decreased when $B_1^+(\mathbf{r})$ was taken into account as a weighting term and pow was increased to prevent the formation of the central hole (as indicated by the ratios displayed on the last row of Fig. 2).

The abovementioned simulations were performed by considering all the voxels belonging to the brain mask.

Reduction of simulation space

Given that the optimization speed is directly related to the number of voxels for which the evaluation was performed, the effect of reducing the number of voxels, N_{vox}, randomly chosen in Ω on the optimization quality was evaluated. After having optimized dynamic k_T-points by considering

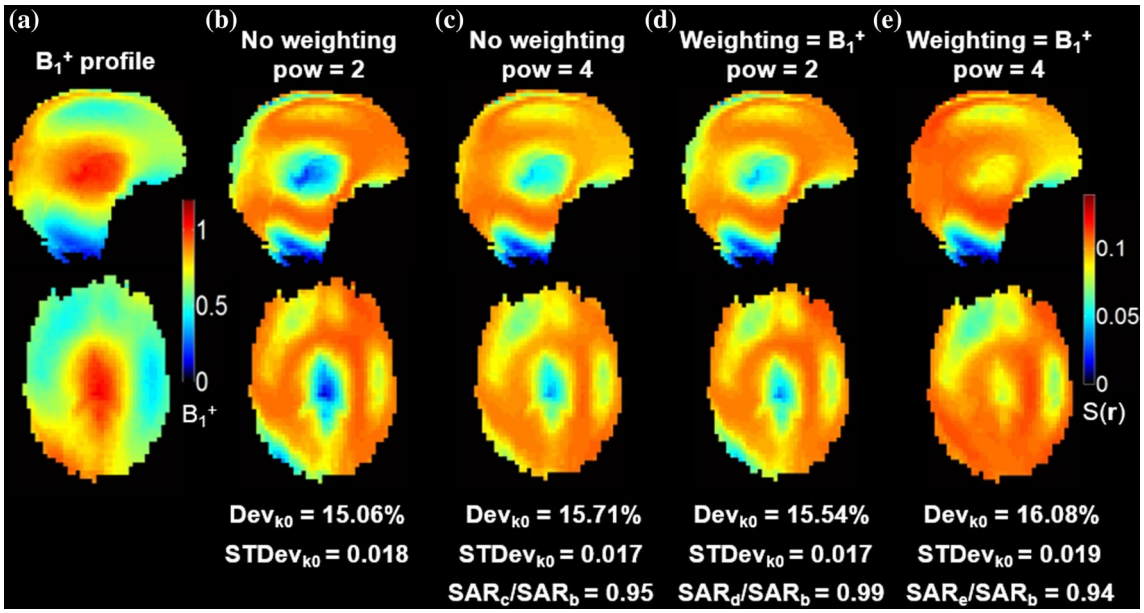

Fig. 2 **a** B_1^+ profile across the brain acquired on subject 1 by using the SA2RAGE sequence. The maps are presented as multiplicative factors of a nominal flip-angle [20]. **b** Magnetization profiles (in arbitrary units) simulated at k-space center using protocol B without weighting factor in Eq. 2 and with a least-squares cost function (pow = 2). The signal hole observed in the center of the brain for the solution found in **b** was corrected by increasing pow up to 4 (**c**, **e**) and/or by adding the B_1^+ profiles as a weighting factor in the cost function (**d**, **e**). The first two rows of numbers on the *bottom* correspond to the deviation in respect to the theoretical signal value expected at k-space center (cf. Eq. 3) and the standard deviation throughout the magnetization profile, respectively. The last row of values show the SAR ratios for the dynamic k_T-points designed in **c**–**e** in respect to those obtained in **b**

all and N_{vox} voxels in Ω, the corresponding solutions $S^{All}(\mathbf{r})$ and $S^{N_{vox}}(\mathbf{r})$ were calculated in the whole space. $S_c^{All}(\mathbf{r})$ and $S^{N_{vox}}(\mathbf{r})$ are the signal profiles simulated at each echo using the SR-EPG. The error E made in respect to the solution obtained when considering all voxels in Ω was calculated using the following expression:

$$E = \frac{1}{ETL}\sum_{c=1}^{ETL}\sum_{r}\frac{\left|\left|\left|S_c^{All}(\vec{r})\right| - \left|S_c^{N_{vox}}(\vec{r})\right|\right|\right|}{\left|\left|S_c^{All}(\vec{r})\right|\right|} \quad (4)$$

As the voxels were randomly selected, $S^{N_{vox}}(\mathbf{r})$ was simulated 20 times such that the average and standard deviation of E could be established.

Figure 3a shows an example where $N_{vox} = 200$ are randomly selected out of the full mask (All = 4070). It can be observed on Fig. 3b that N_{vox} can be significantly reduced while still maintaining a difference smaller than 10 % from the solution found when considering all voxels in Ω. The interquartile range becomes significantly larger when decreasing from $N_{vox} = 200$ to 100, with a sharp increase in the maximum error observed between $N = 500$ and $N = 200$. Figure 3c illustrates how the time required to calculate the dynamic k_T-points decreases when lowering N_{vox}. Figures 3b and c indicated that using $N_{vox} = 500$ for subsequent optimizations was a balanced choice between computational speed and accuracy. At $N_{vox} = 500$ the dynamic k_T-points solution was as precise as when considering all voxels in Ω and the computation time became limited by the number of iterations of the gradient descent algorithm rather than the number of voxels considered. Consequently, the complete design process of the dynamic k_T-points was typically performed in less than 5 min on a standalone PC using Matlab R2012b (The Mathworks).

Dynamic K_T-point evaluation

To evaluate the improvement provided by the dynamic k_T-points over the static k_T-point design and conventional hard pulses, the signal homogeneity (characterized by $STDev_p$) across the echo train was calculated (Fig. 4). The effect of using k_T-points in the 3D TSE sequence on the echo train fidelity (characterized by DEV_p) is also reported in Fig. 4. The ratio of $\sum_{p=1}^{ETL} DEV_p$ between the static k_T-points ($N = 3$) solution over conventional hard pulses k_T-points showed a 12 % improvement in signal fidelity throughout the sequence, whereas a 10 % improvement was obtained when using dynamic k_T-points. This implies that when considering the deviation between the echo profiles and the theoretical signal across the train, similar results were provided by the static and dynamic k_T-points. The optimization procedure using Eq. 2 could have obtained an improvement in DEV_p that had as a bi-product an increase in the inhomogenity of

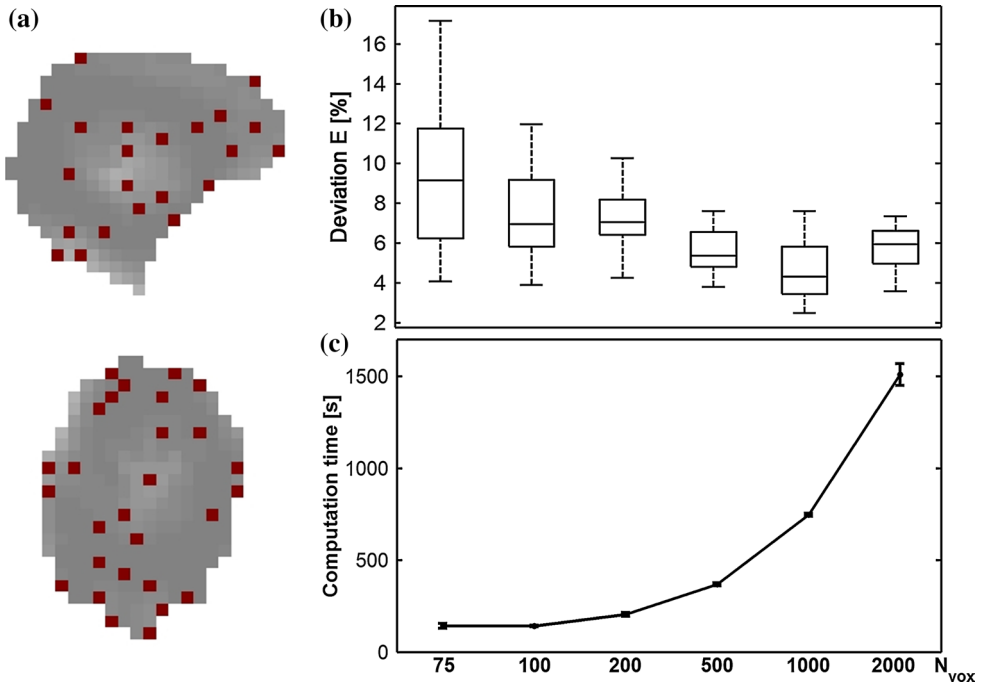

Fig. 3 **a** Sagittal and transversal views of a 64 × 64 × 48 excitation profile downsampled to 4070 voxels. The *red dots* correspond to an example where $N_{vox} = 200$ voxels were randomly selected. **b** Error between the solutions $S^{All}(\mathbf{r})$ and $S^{N_{vox}}(\mathbf{r})$ obtained when performing optimization of dynamic k_T-points (Protocol A, B_1^+ profile of subject 2) by considering N_{vox} randomly chosen voxels in the region of interest Ω vs. all voxels in the same region. The *horizontal line* on each *box* plot represents the median while the *box edges* correspond to the first and third quartiles. The whiskers extend up to the most extreme data points not considered as outliers. **c** Average time (over 20 simulations) required to perform the dynamic k_T-point optimization as a function of N_{vox}

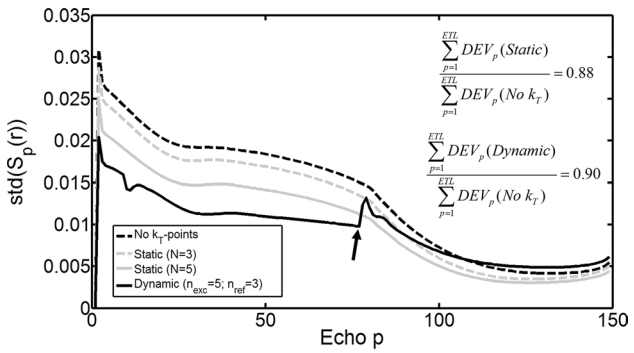

Fig. 4 **a** Assessment of the signal homogeneity by evaluating the spatial standard deviation $STDev_p$ across each echo map $S_p(\mathbf{r})$ for different RF pulse designs. Static k_T-points with $N = 3$ (*dashed grey curve*) and 5 (*solid grey curve*) are compared with dynamic k_T-points designed with $n_{exc} = 5$ and $n_{ref} = 3$ (*solid black curve*). The *black arrow* identifies the transition from steps 4 to 5 of the dynamic k_T-point design process. The results simulated with conventional hard pulses are also displayed (*dashed black curve*). The ratios displayed on the right show the improvements provided by the static ($N = 3$) and dynamic k_T-points with respect to the case simulated with conventional hard pulses on the signal fidelity estimation given in Eq. 3. The same ratios calculated with the $\sum_{p=1}^{ETL} STDev_p$ metric give rise to 0.91 and 0.66 values for the static and dynamic k_T-points, respectively. Those simulations were performed by using protocol C and the B_1^+ profile acquired on subject 4

the solution. This would mean that there would be decreased deviations to the theoretical solution overall, but with increased signal in some regions and decreased signal in other brain regions. Such signal intensity variations imply that the final image would have varying level of T_1- and T_2-weighting. That was clearly not the case as the $\sum_{p=1}^{ETL} STDev_p$ metric, improvements of 9 and 34 % were respectively obtained for the static ($N = 3$) and dynamic k_T-points. This significant difference together with the fact that comparable results were calculated for the $\sum_{p=1}^{ETL} DEV_p$ metric means that T_2-weighted images with improved signal homogeneity can be acquired if dynamic k_T-points are used instead of static ones. When comparing the solid grey and black lines on Fig. 4, it can be seen that the solution resulting from the use of $n_{exc} = 5$ and $n_{ref} = 3$ dynamic k_T-points outperformed the one obtained with $N = 5$ k_T-points in the static regime, in particular for echoes around the k-space center (echo no. 55 for protocol C). Moreover, for the same duration, an SAR drop higher than 60 % was observed when comparing the sequence designed with $n_{exc} = 5$ and $n_{ref} = 3$ dynamic k_T-points to the one with $N = 5$ static k_T-points.

The sudden modulation identified by the black arrow around echo no. 80 in the dynamic k_T-point curve corresponds to the transition from the pulse by pulse optimization (step 4) to the static k_T-point design (step 5), as described

in the methods section. A smoother transition would have been desirable, but this fluctuation was considered acceptable given the computation time benefits and the fact that it corresponds to echoes located in the outer parts of k-space (which should have a limited impact on image quality).

Despite the increased homogeneity obtained using a higher number of k_T-points, images were acquired using 3 k_T-points in the refocusing train, which allowed to keep the RF duration as short as 2.5 ms and still within the SAR limits. Table 1 summarizes the SAR increase resulting from the use of static and dynamic k_T-points with respect to the conventional hard pulses of the same duration as the k_T-point sub-pulses.

Table 1 SAR values for each subject presented as a percentage of the maximum SAR allowed on the single-channel system while using conventional hard pulses, static and dynamic k_T-points

Protocol	SAR^{Hard} (%)	SAR^{Static} (%)	$SAR^{Dynamic}$ (%)
A (subject 2)	15	44	60
B (subject 1)	18	55	95
B (subject 3)	31	78	99
C (subject 4)	29	65	66
C (subject 5)	36	48	53

In the table, the values are presented as a percentage of the SAR limit allowed on the single-channel system.

TSE images acquired with conventional hard pulses, with static k_T-points and with dynamic k_T-points by using protocols A, B, and C showed that for all the protocols used, the effect of the particularly pronounced B_1^+ inhomogeneity observed in the cerebellum as well as in the brain center was increasingly mitigated when static and then dynamic k_T-points were used in the 3D TSE sequence (Fig. 5).

To highlight the improvements in signal and contrast homogeneity observed in the cerebellum (yellow arrows), brain center (green arrows), and temporal lobes (blue arrows) when using k_T-points in the 3D TSE sequence, sagittal, coronal, and transversal images acquired using static and dynamic k_T-points were compared to those obtained with the conventional hard pulses (no k_T-point) (Fig. 6).

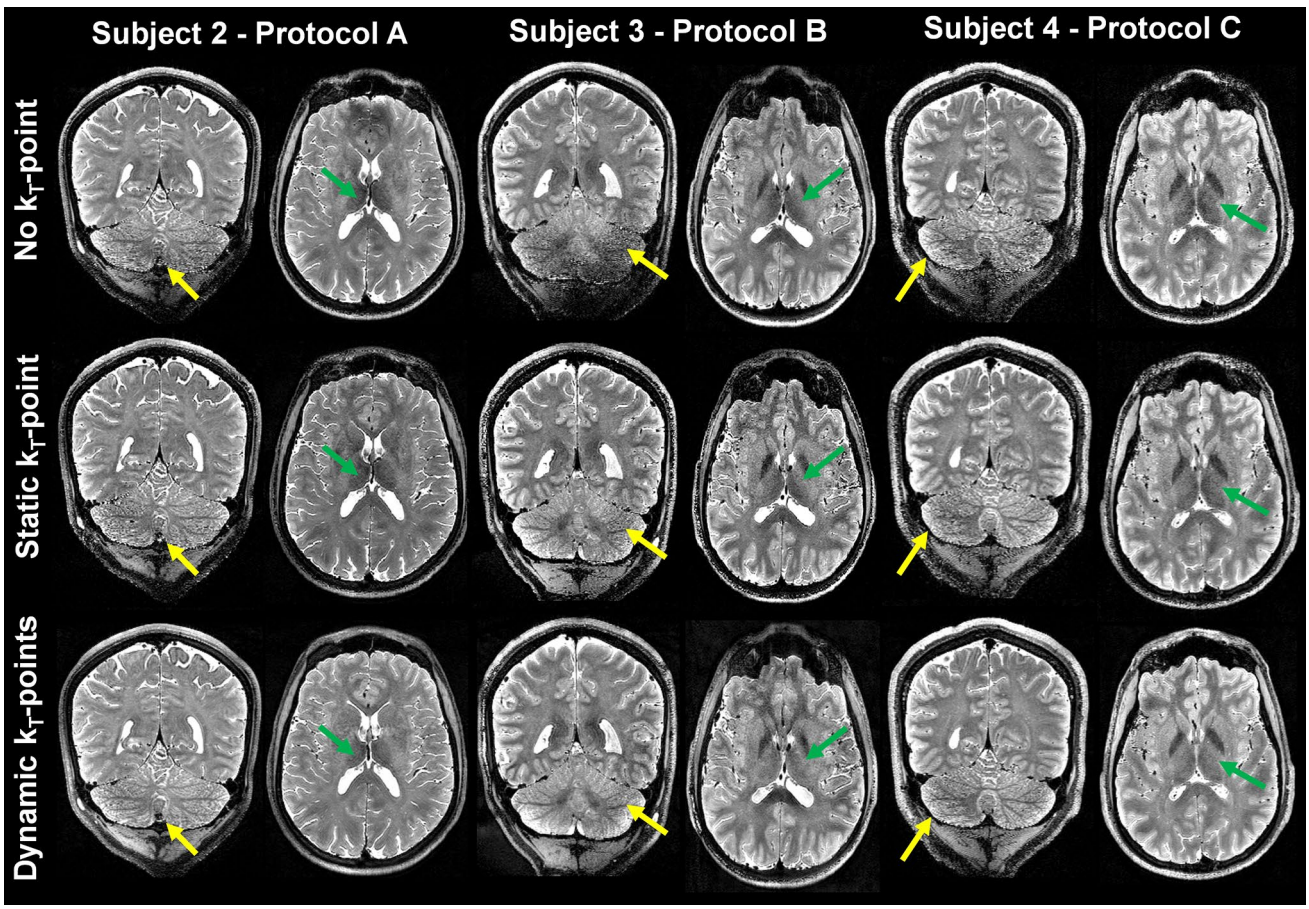

Fig. 5 Coronal and transverse views of 3D TSE images acquired with conventional hard pulses (first row), static (second row) and dynamic (third row) k_T-point pulses using protocols A, B, and C. *Coloured arrows* highlight cerebellar (*yellow*) and central regions (*green*) where the use of static and dynamic k_T-points subsequently provided noticeable improvements. When using dynamic k_T-points, the sub-pulse durations were set to 600 μs (protocol A), 500 μs (protocol B), and 360 μs (protocol C)

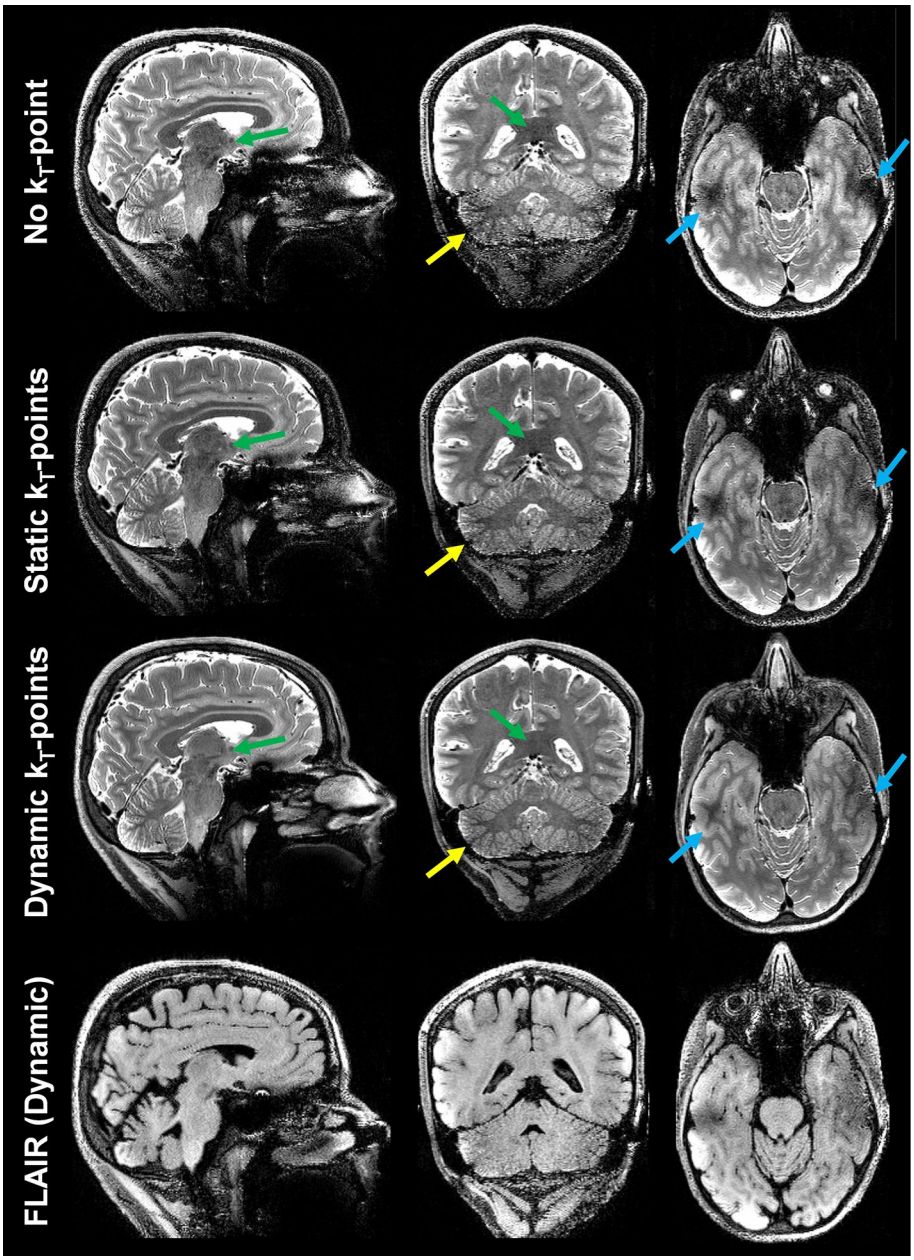

Fig. 6 3D TSE images acquired with conventional hard pulses (first row), static (second row), and dynamic (third row) k_T-points. *Yellow*, *green* and *blue arrows* highlight the significant improvements obtained in the cerebellum, brain center and temporal lobes, respectively. The T_2-weighted images displayed on the first three rows were acquired by using protocol C on subject 5. The dynamic k_T-points were subsequently introduced in the 3D TSE sequence with an inversion preparation module applied at a time TI before the excitation pulse, generating a FLAIR image (*fourth row*)

A higher homogeneity was first observed when static k_T-points were designed, and T_2-weighted images were further improved by using dynamic k_T-points.

The last acquisition demonstrates that FLAIR images with adequate CSF suppression and minimized sensitivity to the common B_1^+ inhomogeneity can be achieved at 7T.

Discussion

The results presented demonstrate that including k_T-points in the SR-EPG formalism can provide a new degree of freedom to control the magnetization distribution in a 3D TSE sequence with variable flip angles leading to T_2-weighted images with a substantially improved level of signal and contrast homogeneity at 7T even without using the parallel transmission technology.

The obtained contrast of the 3D TSE appears reduced when compared to standard 2D TSE [5]. This can be both due to the increased magnetization transfer contrast present on resonance 2D T_2 weighted imaging [6] or to the mixed $T_2 - T_1$ contrast in the presence of the long echo trains used in 3D TSE imaging.

The used cost function (Eq. 2) in our implementation had a strong impact in the obtained results. Using the B_1^+ field as a weighting factor penalizes less signal deviations

in the regions with very low B_1^+ such as those observed close to the neck or temporal lobes and increases the penalty in regions where there is B_1^+ that can be sacrificed for homogeneity purposes. Without this, the algorithm tries to improve the signal homogeneity in regions where there is no B_1^+ available to perform the correction at the cost of signal variations elsewhere. Using a higher power in the cost function simply increases the penalty of large deviations in respect to the target and, therefore, does not lead to the formation of a signal void region. Combining both the power and B_1^+ as a weighting factor was the best penalization tradeoff found and, as displayed in Fig. 2, this phenomenological approach showed to be both quite efficient and reproducible (similar improvements observed for all subjects).

Clearly dynamic k_T-points outperformed static k_T-points in terms of T_2-weighted image quality as evaluated by the signal fidelity and spatial standard deviation metrics (cf. Fig. 4). The large improvements reported in homogeneity found in the simulations are not clearly accessible in the imaging context (after bias field correction), as this metric is mostly ensuring that the degree of T_1- and T_2-weighting is constant throughout the image and that the same level of grey white matter contrast can be observed throughout the image. Although they were not acquired with the same TSE sequence protocol, comparing anatomical images of Fig. 6 (third row) with those presented in [10] (cf. Fig. 6) shows that results almost as good (in terms of signal and contrast homogeneity) as those provided by parallel transmission and static 5 k_T-points can be reached on a single-channel system by using dynamic k_T-points with $n_{exc} = 5$ and $n_{ref} = 3$. When comparing to a similar implementation of dynamic k_T-points using PTx and optimal control, it can be seen that the single-transmit-channel system offers the ability to use longer echo trains, shorter RF pulses and repetition times, ultimately allowing higher-resolution scans to be obtained at a small price in terms of signal homogeneity. In terms of computation time, the methodology presented here is expected to scale linearly with the number of channels, meaning that without an intensive use of parallel computing it would remain unfeasible in practical cases when using standard PTx systems.

It is important to note that for the same number of k_T-points, dynamic k_T-points are usually more SAR demanding than the static design (cf. Table 1 in the "Results" section). For this reason the maximum number of k_T-points for the refocusing pulses was set to $n_{ref} = 3$. By splitting the critical sub-pulses in order to keep the under the RF voltage limit of the scanner, the sequence SAR was minimized to a certain level. Other alternatives to reduce the sequence SAR would have been: (a) a larger k_T-point pulse duration (at a cost of a reduced RF bandwidth and bigger artifacts close to the sphenoid sinus); (b) the introduction of a regularization parameter in the dynamic k_T-point optimization process (at a cost of a higher deviation of the signal in respect to the targeted values); (c) the choice of having variable durations of the sub-pulses, as used in [10]. In the latter option, by simply altering the duration of the sub-pulses for each refocusing pulse, in order to make their amplitudes similar (while keeping all the refocusing pulses with the same duration), the RF power of the k_T-points is minimized. Using such a criterion, the SAR of protocol C could be reduced by as much as 85 %. By implementing the dynamic k_T-points with the condition that all the sub-pulses of a k_T-point pulse have a constant amplitude (and different durations), a larger maximum number of k_T-points would have been acceptable for the same RF duration or alternatively the duration of the RF pulses could have been reduced to 1 ms. This approach was left for future work since the current sequence implementation only allowed one gradient trajectory for all the refocusing pulses with the k_T gradient blips having to be equally spaced.

Future efforts regarding the reduction of the sequence SAR should be complemented with B_0 map integration in the optimization procedure. The current design procedure, with 2.5 ms long dynamic k_T-points, results in dynamic k_T-points solution which approaches the SAR limits. Enforcing the same amplitude on all the sub-pulses would simultaneously reduce the total pulse duration and SAR, but may increase the sensitivity to B_0 variations.

When optimizing static and dynamic k_T-points, the B_0 inhomogeneity over the brain was not considered. To make a fair comparison between the T_2-weighted images acquired with different types of RF pulses, in the conventional case a hard pulse with the same duration as the k_T-point sub-pulses was used while maintaining the same echo spacing (to ensure the same T_2-weighted contrast). In this way, the impact of the B_0 inhomogeneity was similar on images acquired with and without k_T-points, and any improvements observed should be attributed to the B_1^+ compensation mechanism of the k_T-points.

When comparing images acquired with the different RF pulse design strategies (Figs. 5, 6) it is possible to see dramatic signal improvement in the cerebellum (yellow arrows), lower temporal and frontal lobes. In the middle of the brain close to the thalamus, an apparent contrast decrease is observed for subjects 3 and 4 (Fig. 5). This should not be necessarily interpreted as a limitation of the dynamic k_T-point design. In the center of the brain where higher B_1^+ fields exist, the effective echo time will be longer in the case of a design without k_T-point. Hence, the increased contrast in this region is likely to be an effect of the spatial varying T_2-weighting due to B_1^+ inhomogeneity.

New strategies could be envisaged for the methodology presented here; first, when designing dynamic k_T-points, a varying number of sub-pulses could be considered for the

refocusing pulses. In particular, having more k_T-points for pulses bringing the magnetization into the sPSS would help achieving a higher echo signal homogeneity, which could be maintained with fewer k_T-points for the remaining pulses of the sequence. This would improve the T_2-weighted image quality together with a SAR reduction, the overall number of k_T-points of the sequence being lowered.

Second, the k-space points visited by the dynamic k_T-points could also vary from one refocusing pulse of the sequence to the next. This extra degree of freedom could help obtaining better solutions or allow sustaining the same image quality while using more efficient k_T-point pulses. In this work, the gradient blips amplitudes and duration were kept constant for all the refocusing pulses to reduce the computation time and the sequence implementation complexity.

In general, the proposed improvements would aim at increasing the degrees of freedom when optimizing the homogeneity, which should enable the usage of shorter and less SAR-intensive k_T-points, allowing more efficient protocols to be used.

Alternatively, given that B_1^+ maps typically show very reproducible spatial patterns and ranges across subjects with similar head sizes, it could be envisaged to have precomputed dynamic k_T-point solutions computed for various protocols using a B_1^+ map template that could be used on subsequent subjects. This would dramatically decrease the computational burden at the cost of a small reduction on the correction power of the method.

Concerning the experiment workflow, several aspects could still be improved. Currently, the B_1^+ maps were manually transferred to a standalone PC running Matlab, which needed to be informed of the specific protocol to be used (defining the train of variable flip-angles). Once the gradient waveforms and dynamic pulses were computed, these were sent back to the scanner computer. Significant time could be saved by having the k_T-point design routine implemented directly on the scanner computer using a more efficient code and advanced resources such as parallel computation. Such improvements could render the use of the static part of the optimization procedure (step 5) unnecessary, thus avoiding transition artefacts such as those seen on Fig. 4.

Conclusions

It was concluded that replacing the original hard pulses of a 3D TSE sequence with variable flip-angles by dynamic k_T-point pulses allows T_2-weighted images with significantly reduced sensitivity to the B_1^+ inhomogeneity observed at 7T to be acquired with sub-millimeter resolution and acceptable clinical scanning times. Dynamic k_T-points outperform static k_T-points and lead to T_2-weighted images of high quality in terms of signal and contrast homogeneity even on a single-channel transmit system, thereby considerably simplifying hardware, computation and SAR demands.

The methodology presented here was shown to be compatible with FLAIR and could be extended to DIR imaging since those techniques only require the addition of a magnetization preparation module based on adiabatic pulses prior to excitation.

Acknowledgments This work was supported by the Centre d'Imagerie BioMédicale (CIBM) of the University of Lausanne (UNIL), the Swiss Federal Institute of Technology Lausanne (EPFL), the University of Geneva (UniGe), the Centre Hospitalier Universitaire Vaudois (CHUV), the Hôpitaux Universitaires de Genève (HUG), and the Leenaards and Jeantet Foundations. The author would like to thank Wietske van der Zwaag for her help in the management of all the coregistered images present throughout the manuscript.

Compliance with ethical standards

Conflict of interest The authors declare that they have no conflict of interest.

Ethical approval All procedures performed in studies involving human participants were in accordance with the ethical standards of the institutional and/or national research committee and with the 1964 Helsinki declaration and its later amendments or comparable ethical standards.

Informed consent Informed consent was obtained from all individual participants included in the study.

References

1. Fellner C, Menzel C, Fellner FA, Ginthoer C, Zorger N, Schreyer A, Jung EM, Feuerbach S, Finkenzeller T (2010) BLADE in sagittal T_2-weighted MR imaging of the cervical spine. Am J Neuroradiol 31(4):674–681
2. Wattjes MP, Lutterbey GG, Gieseke J, Traber F, Klotz L, Schmidt S, Schild HH (2007) Double inversion recovery brain imaging at 3T: diagnostic value in the detection of multiple sclerosis lesions. Am J Neuroradiol 28(1):54–59
3. Diaz-de-Grenu LZ, Acosta-Cabronero J, Pereira JM, Pengas G, Williams GB, Nestor PJ (2011) MRI detection of tissue pathology beyond atrophy in Alzheimer's disease: introducing T_2-VBM. Neuroimage 56(4):1946–1953
4. Thamburaj K, Radhakrishnan VV, Thomas B, Nair S, Menon G (2008) Intratumoral microhemorrhages on T_2*-weighted gradient-echo imaging helps differentiate vestibular schwannomas from meningioma. Am J Neuroradiol 29(3):552–557
5. Trampel R, Reimer E, Huber L, Ivanov D, Heidemann RM, Schafer A, Turner R (2014) Anatomical Brain Imaging at 7T Using Two-Dimensional GRASE. Magn Reson Med 72(5):1291–1301
6. Norris DG, Boyacioglu R, Schulz J, Barth M, Koopmans PJ (2014) Application of PINS radiofrequency pulses to reduce power deposition in RARE/turbo spin echo imaging of the human head. Magn Reson Med 71(1):44–49

7. Madelin G, Oesingmann N, Inglese M (2010) Double Inversion Recovery MRI with fat suppression at 7 tesla: initial experience. J Neuroimaging 20(1):87–92
8. Visser F, Zwanenburg JJ, Hoogduin JM, Luijten PR (2010) High-resolution magnetization-prepared 3D-FLAIR imaging at 7.0 Tesla. Magn Reson Med 64(1):194–202
9. Zwanenburg JJ, Hendrikse J, Visser F, Takahara T, Luijten PR (2010) Fluid attenuated inversion recovery (FLAIR) MRI at 7.0 Tesla: comparison with 1.5 and 3.0 Tesla. Eur Radiol 20(4):915–922
10. Eggenschwiler F, O'Brien KR, Gruetter R, Marques JP (2014) Improving T_2 -weighted imaging at high field through the use of kT -points. Magn Reson Med 71(4):1478–1488
11. Cloos MA, Boulant N, Luong M, Ferrand G, Giacomini E, Le Bihan D, Amadon A (2012) kT -points: short three-dimensional tailored RF pulses for flip-angle homogenization over an extended volume. Magn Reson Med 67(1):72–80
12. Malik SJ, Padormo F, Price AN, Hajnal JV (2012) Spatially resolved extended phase graphs: modeling and design of multipulse sequences with parallel transmission. Magn Reson Med 68(5):1481–1494
13. Massire A, Vignaud A, Robert B, Le Bihan D, Boulant N, Amadon A (2014) Parallel-transmission-enabled three-dimensional T-weighted imaging of the human brain at 7 Tesla. Magn Reson Med 73(6):2195–2203
14. Alsop DC (1997) The sensitivity of low flip angle RARE imaging. Magn Reson Med 37(2):176–184
15. Hennig J (1988) Multiecho imaging sequences with low refocusing flip angles. J Magn Reson 78(3):397–407
16. Ma C, Xu D, King KF, Liang ZP (2011) Joint design of spoke trajectories and RF pulses for parallel excitation. Magn Reson Med 65(4):973–985
17. Eggenschwiler F, Gruetter R, Marques JP (2013) Large tip angle kT-points based on a linearization of the Bloch equations. In: Proceedings of the 21st Annual Meeting of ISMRM, Salt Lake City, USA
18. Teeuwisse WM, Brink WM, Haines KN, Webb AG (2012) Simulations of high permittivity materials for 7 T neuroimaging and evaluation of a new barium titanate-based dielectric. Magn Reson Med 67(4):912–918
19. Teeuwisse WM, Brink WM, Webb AG (2012) Quantitative assessment of the effects of high-permittivity pads in 7 Tesla MRI of the brain. Magn Reson Med 67(5):1285–1293
20. Eggenschwiler F, Kober T, Magill AW, Gruetter R, Marques JP (2012) SA2RAGE: a new sequence for fast B_1^+-mapping. Magn Reson Med 67(6):1609–1619
21. Zhang Y, Brady M, Smith S (2001) Segmentation of brain MR images through a hidden Markov random field model and the expectation-maximization algorithm. IEEE Trans Med Imaging 20(1):45–57